applied sciences

MDPI

Article

The Dynamic Coupling Analysis for All-Wheel-Drive Climbing Robot Based on Safety Recovery Mechanism Model

Fengyu Xu [1,2], Quansheng Jiang [3,*], Fan Lv [1], Mingliang Wu [4] and Laixi Zhang [4]

1 College of Automation, Nanjing University of Posts and Telecommunications, Nanjing 210003, China; xufengyu598@163.com (F.X.); lvfan6514@163.com (F.L.)
2 State Key Laboratory of Robotics and System (HIT), Harbin Institute of Technology, Harbin 150001, China
3 School of Mechanical Engineering, Suzhou University of Science and Technology, Suzhou 215009, China
4 School of Mechanical & Electronical Engineering, Lanzhou University of Technology, Lanzhou 730050, China; wml10757@163.com (M.W.); laixi_zh@163.com (L.Z.)
* Correspondence: qschiang@163.com; Tel.: +86-512-6832-0622

Received: 9 September 2018; Accepted: 30 October 2018; Published: 1 November 2018

Abstract: Cable is one of the most important parts on cable-stayed bridges. Its safety is very important. The aim of this study is to design an all-wheel-drive climbing robot based on safety recovery mechanism model for automatic inspection of bridge cables. For this purpose, a model of a three-wheel-drive climbing robot with high-altitude safety recovery mechanism is constructed and the basic performances such as climbing ability and anti-skidding properties are analyzed. Secondly, by employing the finite element method, natural frequency of the robot is calculated and that of a cable with concentrated masses is obtained through use of the Rayleigh quotient. Based on the mentioned quantities, the dynamic characteristics of the robot–cable system are further analyzed. In order to verify the climbing ability of the designed robot, a prototype of the robot is made, a robot testing platform is established and the climbing & loading experiments of the robot are carried out. The experiment results illustrated that the robot can carry a payload of 10 kg and safely return along the cable under the influences of inertial force.

Keywords: climbing robot; safety recovery mechanism; cable detection; dynamic coupling analysis

1. Introduction

A cable-stayed bridge is a common structural form. The cables which are as important bearing parts of the bridge, need to be inspected regularly due to the influences of extreme conditions, such as wind- and rain-induced vibration. At present, manual detection methods are widely used. This study designs a robot to replace workers for cable defect detection tasks.

Robots for cable detection are non-standard automated items of equipment and many researchers have proposed various innovative mechanisms therein: for example, Cho et al. used a six-wheel robot for bridge cable inspection [1,2]. Such a robot can adjust its clamping forces according to the situation encountered on the surface of a cable, so as to adapt to cables of different diameters. Moreover, they designed a cable visual detection system and took pictures of the cable surface from different directions with three cameras. The pictures were sent to the ground-based monitoring station in real-time. Park et al. designed a cable crawling robot [3,4]. The cables are automatically monitored by using non-destructive testing (NDT) technology. With the development of an eight-channel sensor for magnetic flux leakage inspection, the measured magnetic field signals were transformed into 3-d graphics to allow intuitive monitoring. Ho et al. proposed a robot for cable detection [5]. By combining it with an efficient image-based damage detection system, the damage to the cable surface was

automatically recognized through image processing and pattern recognition technology. Type-I and -II robots for cable maintenance are capable of carrying 250 kg payloads and designed by Luo Jun et al., which have been tested on Xupu Bridge in Shanghai, China for maintenance issues such as the painting of bridge cables [6].

There are a lot of researches on bar and pipeline climbing robots. For instance, Mahmoud et al. proposed a 3D CLIMBER bar climbing robot that can climb along a spatial tubular structure [7]. The 3D CLIMBER can measure position deviations against three different classifications by using a sensor and then the errors therein are corrected one-by-one. Zhu et al. proposed a method of computing operational regions for transition in global path searching for biped climbing robots [8]. Furthermore, Mahmoud et al. designed an oil and gas pipeline climbing robot to detect bent pipelines and T-shaped oil and gas pipelines [9]. Allan et al. developed a wheeled bar climbing robot which is capable of climbing along a straight bar with heavy payloads [10]. Li Nan et al. designed a climbing robot that can move along the bar and rotate around it [11]. In addition, Lam et al. investigated a Treebot climbing robot with two claws [12]: when the robot climbs a tree, it detects the position of the trunk based on the information provided by an encoder, a contact sensor and an inclinometer to deduce the optimal climbing path. Schempf proposed a series of robots for pipeline detection and designed corresponding NDT methods [13]. Guan proposed the use of a climbing robot with two claws [14]. By using three sensors (laser range scanner, color camera and ultrasonic ranging module) the deviation of different poses of the holder at the end is detected and then corrected step-by-step, thus realizing automatic gripping and grasping. A grasping module of cross-arranged claw is designed for the inspection of rough stone and concrete wall surfaces, which performs well in grasping vibrating walls with certain anti-rollover capability [15]. Yanagida et al. designed a shape shifting rolling–crawling–wall-climbing robot with wall-climbing locomotion abilities [16]. Xu et al. designed a robot for cable inspection with double wheels on both sides [17,18]. Such a robot can overcome the influences of high-altitude wind loads and conduct NDT by entering the high-altitude inclined cable environment well beyond human reach. An energy saving and recovery method based on the theory of counter electromotive force was proposed to realize the energy-saving recovery of robots at an altitude of hundreds of meters. The author also analyzed the anti-dynamic ability of the climbing robot based on the claws [19].

Other representative climbing robots for low-altitude operation are described as follows: one is a robot with claws, designed by Moon, that can span between interlaced bars [20]. The other is a humanoid wheeled climbing robot designed by Ahmadabadi, that moves under joint control of two motors and the clamping principle lies between spring-loaded-type and squirmy-type-designs [21]. Such a robot is used for cleaning street lamps on high-speed roads. In addition, for some wall climbing robots, their adhesion principle provides some inspirations for cable detection robots. For example, the robot with vacuum suckers designed by Lee [22] and a wheeled robot designed by Espinoza adopt vacuum adhesion and magnetic adhesion devices [23]. They show simple principles and could be easily controlled. Furthermore, the robots can move freely on arc-shaped walls and operate in various environments, such as pipelines and walls of pipelines.

In conclusion, researchers have studied the use of robots for cable inspection, while the dynamic characteristics of such robots are rarely touched. The reasons for this include the following facts: robot climbing can change the vibration characteristics of cables themselves and cable vibration influences the climbing ability of the robot. Therefore, we proposed a new all-wheel-drive climbing robot and solved the dynamic problems in robot–cable coupling. The research is structured as follows: Section 2 summarizes models of all-wheel-drive climbing robot based on safety recovery mechanism according to the needs of cable inspection at high altitude. Section 3 covers the analysis of its basic climbing performance. Coupling dynamic characteristics of the robot–cable system are studied in Section 4. Section 5 covers the fabrication of the prototype climbing robot and its testing platform, with which the testing and analysis of climbing performance are conducted. Finally, Section 6 summarizes the research and outlines the future research work.

2. Structural Model of the Climbing Robot

Firstly, the mechanical structure including climbing principle and specific driving structure of the robot was introduced. Secondly, a centrifugal–friction recovery mechanism was introduced and the key factors influencing braking ability were analyzed through simulation.

2.1. Overall Scheme for the Climbing Robot

The proposed robot involved the clamping of a cable clamped with three wheels. According to the principle illustrated in Figure 1a, wheels A and C were set on the left and right support plates which are opposite to each other, while wheel B was set on the left and right swing plates in an opposed arrangement. Swing plates and support plates were hinged and rotated freely around the hinge, while the spring mechanism pushed the upper and lower support bars and thus the robot clamping cables. The shapes of support plates and swing plates are shown in Figure 1b. Motors 1 and 2 directly drove wheels A and B through the synchronous belt drive and wheel C was driven by motor 1 through another synchronous belt, thus forming the all-wheel-drive climbing robot (Figure 2).

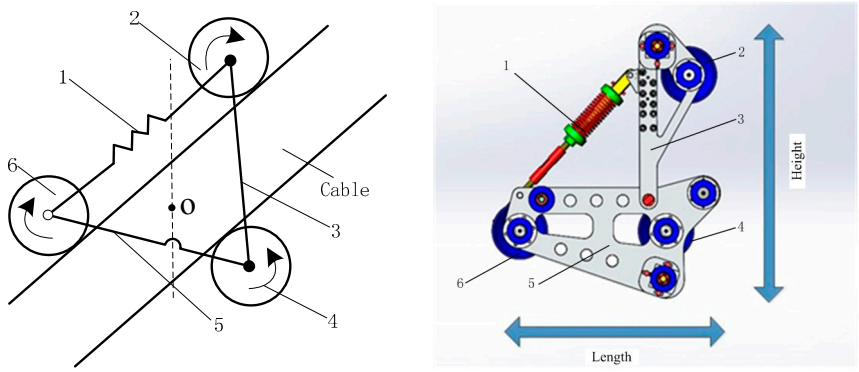

(**a**) (**b**)

Figure 1. The model of climbing robot. 1—Spring mechanism; 2—Wheel B; 3—Swing plate; 4—Wheel A; 5—Support plate; 6—Wheel C. (**a**) The principle of the climbing robot; (**b**) Left view of the robot.

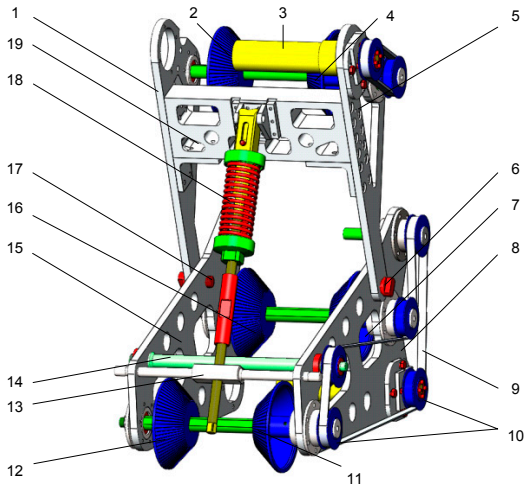

Figure 2. The structure of the climbing robot. 1—Left swing plate; 2—Left half-wheel B; 3—Motor 2; 4—Right half-wheel B; 5—Right swing plate; 6—Right hinge; 7—Right half-wheel A; 8—Right support plate; 9—synchronous belts; 10—Synchronous pulley; 11—Right half-wheel C; 12—Left half-wheel C; 13—Lower support bars; 14—stop lever; 15—Left support plate; 16—Left half-wheel A; 17—Left hinge; 18—Spring mechanism; 19—Upper support bars.

Each of the three rolling wheels were comprised of two half-wheels on the left and right (Figure 2), which allowed easy adjustment of the distance between the two half-wheels and the clamping force. All parts of the robot were set between the left and right support plates.

Based on the joint effects of the relative rotation of swing plates and support plates, scaling of the spring and adjustment of spacing of rolling wheels, the robot clamped the cable. In practical applications, it is more convenient to adjust clamping forces by adjusting the spacing of the rolling wheels, so the design allowed for a mass of 11 kg and a length ranging from 370 mm to 400 mm. Moreover, the width was 236 mm and the height was able to be adjusted within the range from 410 to 440 mm.

2.2. The Safety Recovery Mechanism Model of the Climbing Robot

When electrical failure occurs, the robot freely falls to the ground from high altitude and the fast rate of descent and impact velocity damages the equipment and even threatens the safety of workers. In order to avoid fast gliding speed of the robot after electrical failure, a centrifugal–friction recovery mechanism was designed. The braking force was dynamically adjusted in accordance with different inclination angles of cables as shown in Figure 3a. The recovery mechanism consisted of mass blocks, a brake disc, a friction plate, a gearbox and a rotary shaft (Figure 3b–d) and each part was set on the rotary shaft. The chute was processed on one side of the brake disc and mass blocks slid in the chute to push the brake disc to overcome the spring force and then move along the rotary shaft. The brake disc contacted with the friction plate to generate braking torque, while the gearbox generated an acceleration to increase the braking torque of the friction plate on the robot.

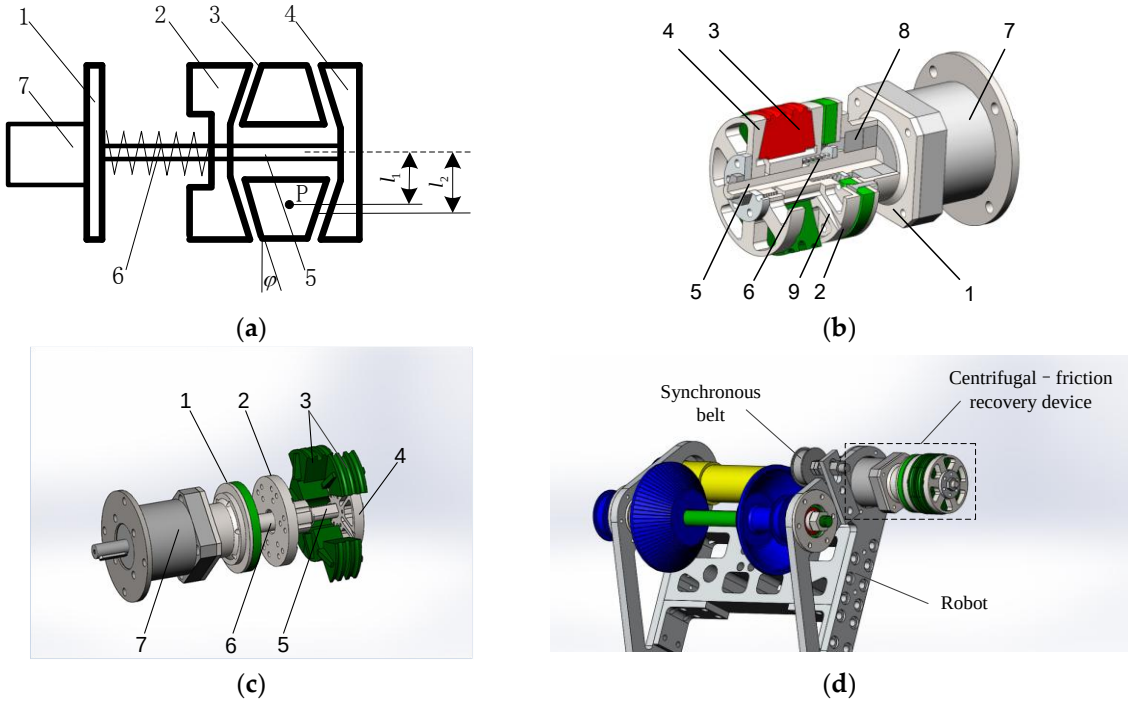

Figure 3. Safety recovery structure of the robot. 1—Main case; 2—Brake disc; 3—Mass blocks; 4—Base; 5—Rotary shaft; 6—Spring mechanism; 7—Gearbox; 8—Ball bearing; 9—slideway. (**a**) Schematic diagram of recovery mechanism; (**b**) The inner structure of the recovery device; (**c**) Breakdown drawing of recovery mechanism; (**d**) Centrifugal–friction recovery mechanism.

When the descent speed of the robot is low, the brake disc is separated from the friction plate under the effects of the spring (Figure 4a). If the robot drops quickly after a power outage, the mass blocks slide outside under the effects of centripetal forces and the axial component thereof overcomes

the spring forces, so that the brake disc makes complete contact with the friction plate and braking forces are dynamically transferred to the robot (Figure 4b).

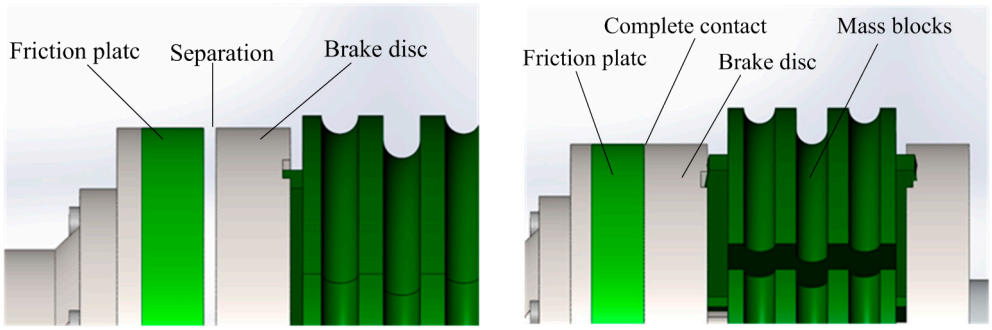

Figure 4. Movement state of the recovery mechanism. (**a**) Low-speed movement of the robot; (**b**) High-speed movement of the robot.

With the changes of descent speed of the robot, contact forces between the friction plate and brake disc changes constantly. In theory, the braking torque can automatically reach a stable value according to the inclination angle of cables and loads on the robot.

Both sides of mass blocks are designed for a certain inclination angle φ so as to transform the centripetal force into an axial force. The component of this force in the axial direction of the sum of centripetal forces of six mass blocks can be expressed as:

$$F = 3 \cdot m \cdot w^2 \cdot l_1 \cdot \cot \varphi \tag{1}$$

where m, w and l_1 represent the mass of mass blocks, the angular velocity of the rotary shaft and the distance from the center (Point P) of gravity of the mass blocks to the axis of the rotary shaft, respectively. If small changes in the spring forces of the brake in working are ignored, axial force can be expressed as:

$$\begin{cases} F' = 0 & (F_{t1} > F) \\ F' = F - F_{t1} = 3 \cdot m \cdot w^2 \cdot l_1 \cdot \cot \varphi - F_{t1} & (F_{t1} < F) \end{cases} \tag{2}$$

where F_{t1} denote the spring force. The braking torque thus generated is:

$$M' = F' \cdot \mu_f \cdot l_2 = (3 \cdot m \cdot w^2 \cdot l_1 \cdot \cot \varphi - F_{t1}) \cdot \mu_f \cdot l_2 \tag{3}$$

where μ_f denote the coefficient of friction. l_2 represents the distance from the geometrical center of the mass blocks to the axis of the rotary shaft. When the robot runs at a high speed, it needs to satisfy the following equation in order to limit the speed and move more uniformly in a certain range:

$$i \cdot M' = M \tag{4}$$

where i is the gear ratio and M is the driving torque during the descent of the robot, thus giving the angular speed of the rotary shaft:

$$w = \sqrt{\left(\frac{M}{\mu_f l_2 \cdot i} + F_{t1}\right) \Big/ (3 \cdot m \cdot l_1 \cdot \cot \varphi)} \tag{5}$$

The descent speed of the robot is:

$$v = \frac{1}{i} w \cdot d \tag{6}$$

where d represents the diameter of rolling wheels of the robot and the falling torque M can be expressed as:

$$M = G \cdot \cos\beta \cdot d \tag{7}$$

where G indicates the self-weight of the robot and β is the angle of inclination of cables, so the descent speed of the robot can be rewritten as:

$$w = \sqrt{\left(\frac{M}{\mu_f l_2 \cdot i} + F_{t1}\right) \Big/ \left(3 \cdot m \cdot l_1 \cdot \cot\varphi\right)} \tag{8}$$

According to Equation (8), by adjusting gear ratio and spring force, the descent speed of the robot can be changed. Assuming that the friction coefficient is $\mu = 0.5$, the mass of the sliding block is $m = 0.2$ kg, the inclination angle at the both ends of sliding block is $\varphi = 10^\circ$, the distance from the center of gravity of the sliding block to the axis is $l_1 = (16\text{–}20)$ mm and $l_2 = (18\text{–}22)$ mm. Furthermore, all the values of l_1 and l_2 are changeable in the process of the robot landing. To simplify the process of calculation, the maximum values are used in the simulation. At last, the relationship linking the gear ratio, spring force and descent speed is shown in the simulation diagram.

As shown in Figure 5a, the spring force does affect braking ability (although only slightly), while the influence of the gear ratio is greater. Furthermore, by setting the spring force is 30 N and setting gear ratio is 10, the effects of the mass of the robot and the inclination angle of cables on the rate of descent were studied. Let the mass changes between 10 kg and 80 kg and the inclination angle of cables vary from 0° to 80°, Figure 5b shows the influences of inclination angle of the cables on braking force is far greater than that of the mass of the robot. Therefore, the designed recovery mechanism has more obvious effects on cables with larger inclination angles.

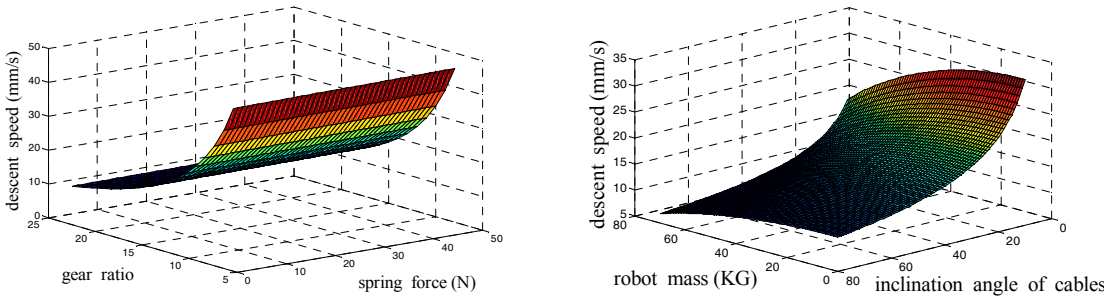

(**a**) (**b**)

Figure 5. Simulation diagram of descent speed. (**a**) Relationship of descent speed, gear ratio and spring force. (**b**) Relationship of descent speed, robot mass and inclination angle of cables.

3. Analysis of Climbing Performance for the Climbing Robot

This section mainly analyzed the basic conditions for robot climbing and basic mechanical performance, such as the minimum output torque of the motors and the minimum friction force on the rolling wheels to prevent skidding. The robot was driven by two motors. In the schematic diagram, the driving wheels (A and B) are represented by solid circles, while the center of wheel C is indicated by a hollow circle. Moreover, wheel C is jointly driven by the motor installed on wheel A through a synchronous belt.

3.1. Analysis of Climbing Ability

The climbing robot utilizes the spring mechanism to provide force to clasp the cable and the driving wheel is actuated by DC motor to roll along the cable. The friction force must be greater than the gravity of the robot and payloads, so that it can climb along the cables inclined at any angle. The climbing principle, coordinate system and external force analysis are shown in Figure 6. For the whole

robot mechanism, if the motor with enough input torque is used, we can establish the equilibrium equation:

$$\begin{cases} F_{fa} + F_{fb} + F_{fc} = Mg\cos\beta \\ N_b + N_c = N_a + Mg\sin\beta \end{cases} \tag{9}$$

where $F_{fa} = N_a\mu$, $F_{fb} = N_b\mu$, $F_{fc} = N_c\mu$, denote the maximum static friction force of the three wheels. N_a, N_b, N_c represent the supporting force of the three wheels, μ is static friction coefficient. M, g, β and O represent the mass of the robot including external payloads, the gravitational acceleration, the inclination angle of the cable and the center of gravity of the robot, respectively.

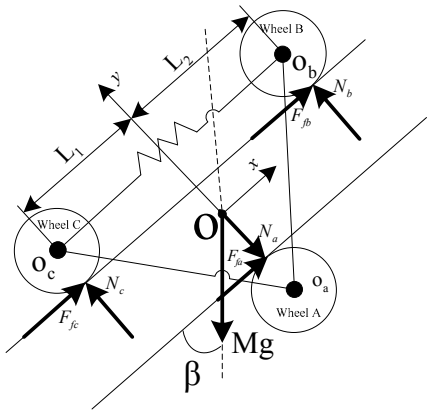

Figure 6. Climbing principle.

In this paper, various obstacles on cable surfaces are neglected. Meanwhile, by ignoring small losses during the drive and regarding the sum of output torques of driving wheels as τ, the following balance equation can be established:

$$\tau = (F_{fa} + F_{fb} + F_{fc}) \cdot r = Mg \cdot \cos\beta \cdot r \tag{10}$$

where r represents the equivalent radius of the rolling wheels.

As the two motors drive three groups of rolling wheels, in ideal conditions, the single actual friction torque t' of rolling wheels is as follows in ideal conditions:

$$\tau' = \frac{1}{3}Mg \cdot \cos\beta \cdot r \tag{11}$$

In addition, in order to prevent skid in climbing, the sum F_f of the minimum sliding frictions of the rolling wheels must satisfy: $F_f > Mg \cdot \cos\beta$.

Suppose the velocity of the robot is v and the efficiency of the motor is η. In the design process, we should choose a driving wheel that possesses a rather large friction coefficient with the cable to reduce the clasped force. Here, ignore the inner friction of the robot, which the required whole power of DC motor P is:

$$P = F_f v/\eta = \frac{Mgv \cdot \cos\beta}{\eta} \tag{12}$$

3.2. Anti-Skid Analysis in Operating Conditions

Skid results from the lack of friction force between rolling wheels and cables, while friction is mainly transformed from the force generated by the spring. To study the relationship between spring force and friction force, some assumptions were made as follows: (1) The robot is climbing on a smooth cable without any obstacles in a constant velocity. For the wheel with the smallest support force, the driving torque of the motor equals the torque produced by the tangential friction forces. (2) All the driving motors are the same, therefore, we suppose the robot reached the maximum load when the

wheel with smallest support force is in the slipping state. (3) To simply the calculation, the self-weight of the swing plate is ignored as it has less effect on the robot climbing ability. That is to say, the two sets of robot swing plates are considered as two two-force bars. (4) All the inner frictions of the robot mechanism are ignored. According to Figures 6 and 7, which shows the schematic diagram of the movement of the robot, the balance equations of the three groups of rolling wheels are established.

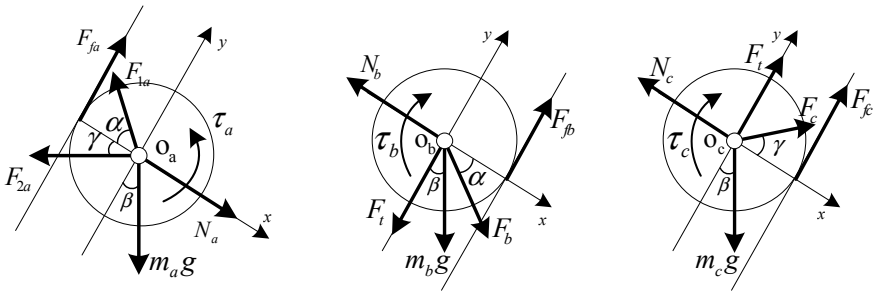

Rolling wheel A Rolling wheel B Rolling wheel C

Figure 7. Force balance relationships of rolling wheels.

In Figure 7, α and γ indicate the angles of two-force bars with the horizontal direction respectively and F_t represents the spring force. N_a, N_b and N_c are the support force, which denote the constraint reactions of cables on rolling wheels, while F_{1a}, F_b, F_{2a} and F_c denote forces acting on the bars of the rolling wheels. According to the nature of two-force bars, it is obvious that $F_{1a} = F_b$, $F_{2a} = F_c$:

As presented in Figure 7, the forces on rolling wheels A, B and C are presented, so the force balance equation for rolling wheel A is

$$\begin{cases} N_a + m_a g \sin\beta = F_{1a}\cos\alpha + F_{2a}\cos\gamma \\ F_{fa} + F_{1a}\sin\alpha = F_{2a}\sin\gamma + m_a g\cos\beta \\ \tau_a = F_{fa} r \end{cases} \tag{13}$$

For the rolling wheel B we have

$$\begin{cases} N_b = F_b\cos\alpha + m_b g\sin\beta \\ F_{fb} = F_b\sin\alpha + F_t + m_b g\cos\beta \\ \tau_b = F_{fb} r \end{cases} \tag{14}$$

Therefore we can get: $N_b = \frac{F_t - m_b g\sin\beta tg\alpha + m_b g\cos\beta}{\mu - tg\alpha}$, For the rolling wheel C

$$\begin{cases} N_c = F_c\cos\gamma + m_c g\sin\beta \\ F_{fc} + F_t + F_c\sin\gamma = m_c g\cos\beta \\ \tau_c = F_{fc} r \end{cases} \tag{15}$$

Therefore we can deduce: $N_c = \frac{-F_t + m_c g\sin\beta tg\gamma + m_c g\cos\beta}{\mu + tg\gamma}$, For the whole robot (Figure 6):

$$\begin{cases} N_a + Mg\sin\beta = N_b + N_c \\ F_{fa} + F_{fb} + F_{fc} \geq Mg\cos\beta \\ F_{fa} r + N_b L_2 = N_c L_1 + F_{fb} r + F_{fc} r \end{cases} \tag{16}$$

In the above equations, F_{fa}, F_{fb} and F_{fc} represents the friction force of three rolling wheels respectively. m_a, m_b and m_c represents the mass of three rolling wheels. τ_a, τ_b and τ_c represents the torques acted on three rolling wheels. μ denotes the friction coefficient between the rolling wheels and the cable surface.

Therefore we can get: $N_a = N_b + N_c - Mg\sin\beta$. Combining Equations (13)–(16), the following constraint equation is obtained:

$$\begin{cases} N_a = N_b + N_c - Mg\sin\beta \\ N_b = \frac{F_t - m_b g\sin\beta tg\alpha + m_b g\cos\beta}{\mu - tg\alpha} \\ N_c = \frac{-F_t + m_c g\sin\beta tg\gamma + m_c g\cos\beta}{\mu + tg\gamma} \end{cases} \tag{17}$$

For the three rolling wheels, we conclude the supporting force of the wheel C is the smallest one from the results the numerical analysis. Therefore, wheel C slides first. For wheel C climbing on the cable vertical cable ($\beta = 0^\circ$), we suppose it is the critical state when $F_{fc} = N_c \cdot \mu$. The motor whose rated torque $\tau_c = F_{fc} r$ is chosen as the source of power. Because all the driving motors are the same, that means $\tau_a' = \tau_b' = \tau_c'$, so $F_{fa} = \frac{\tau_a'}{r}$, $F_{fb} = \frac{\tau_b'}{r}$ is deduced. Here, τ_a', τ_b', τ_c' represents the rated torque of the driving motors. Therefore, the maximum friction of the robot meet $F_f = 3F_{fc} \geq Mg \cdot \cos\beta$.

To study climbing performance of the robot under the condition of cable vibration, it is assumed that the robot is affected by inertial force during the vibration and simple harmonic vibration is applied to the cables with a vibration amplitude and frequency of 0.01 m and 10 Hz. Moreover, $\alpha = \gamma = 45^\circ$, $\beta = 0^\circ$ and friction coefficient $\mu = 0.5$, $m_a = m_b = m_c = 0.5$ kg. On this basis, the changes in friction force provided by the robot under cable vibration are simulated, as shown in Figure 8. The blue curves represent the maximum static friction force the cable exerted on the wheel, while red curves (Figure 8a–c) indicate the maximum (critical) friction force the motor exerted on the wheel. From the figures, the maximum static friction force is larger than the climbing force generated by the motor. Therefore, all the three wheels did not slide. Figure 8d shows the sum of the three driving force. The robot can take 15 kg payload besides self-weight. In accordance with Formula (17) and simulation results, the minimum spring force F_t is 130 N when the wheel C did not slide. To guarantee the robot climbs in a stable manner on the cable, the suitable scope of spring force is 130 N–150 N.

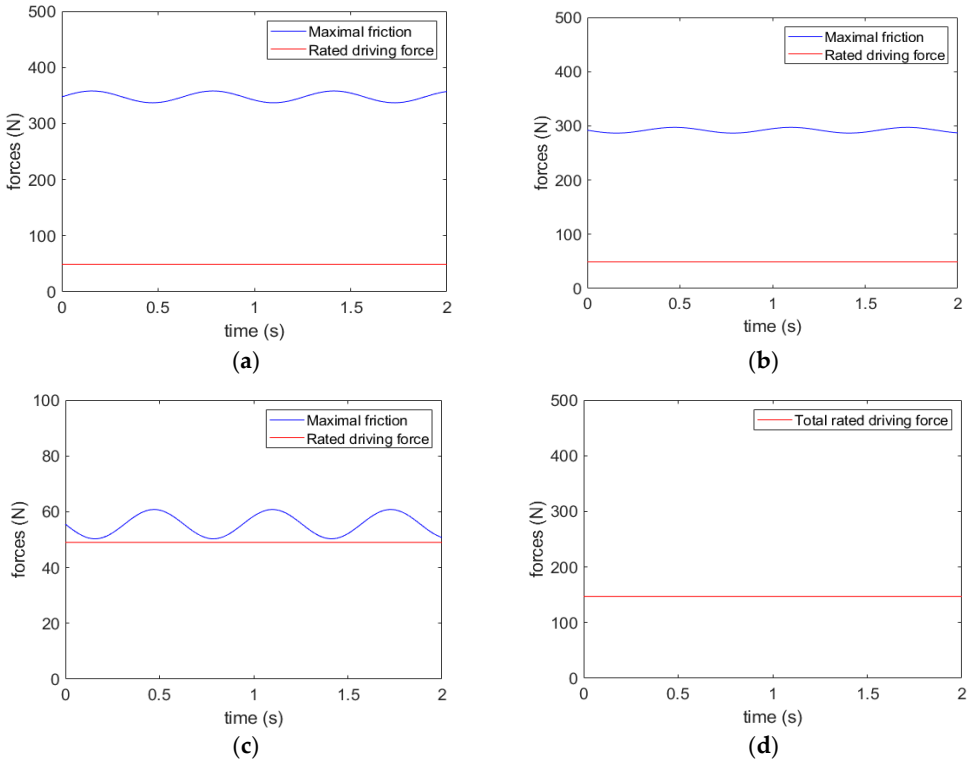

Figure 8. Changes in friction forces on the rolling wheels. (**a**) Rolling wheel A; (**b**) Rolling wheel B; (**c**) Rolling wheel C; (**d**) The payload of the robot.

4. Dynamic Characteristics of the Robot–Cable System

When the robot climbs the cable, once resonance occurs, the safety of the cable is affected. By using the finite element method, the natural frequency of the robot rack is estimated and then natural frequency of the cable is obtained with Rayleigh quotient. Finally we analyze the dynamic characteristics of the robot–cable system.

4.1. Natural Frequency of the Climbing Robot

By modeling the robot rack, the robot includes the following parts, such as an aluminum alloy rack, steel wheel shafts, rolling wheels and a spring. Owing to the rack contributing most to the weight of the robot and as the elastic modulus of steel is much larger than that of aluminum alloy, the aluminum alloy rack is the key component here. The parameters of the robot are illustrated in Table 1. By removing some holes and slots that slightly affect the overall structure and replacing the motor with a lumped mass of 0.7 kg, the finite element model of the robot is obtained (Figure 9).

Table 1. The parameters of the robot.

Item	Value
Length	370~400 mm
Width	236 mm
Height	410~440 mm
Material	Aluminum Alloy
Gravity	11.7 kg

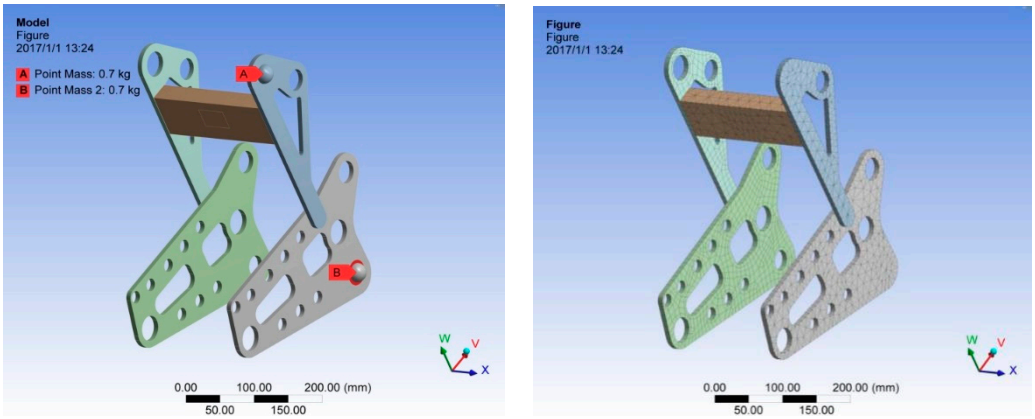

(**a**) (**b**)

Figure 9. Finite element analysis of the robot. (**a**) Finite element model of the robot; (**b**) Finite element mesh.

The fixed constraints were applied on wheel shafts and the spring and the model was divided into grids measuring 10 mm. Through modal analysis, the first five orders of natural frequencies of the robot rack are 322 Hz, 463 Hz, 606 Hz, 723 Hz and 911 Hz.

4.2. Analysis of the Natural Frequency of the Cable

The string vibration equation is used to describe cable vibration (Figure 10). Owing to the robot climbing on a long cable, which has certain influences on cable vibration, the robot is regarded as a point mass to establish a string vibration equation with this lumped mass:

$$\begin{cases} u_{tt} - a u_{xx} = 0 & x \neq x_0 \\ u_{tt} - a_{x0} u_{xx} = 0 & x = x_0 \end{cases} \tag{18}$$

where x_0, l and u represent the position of the robot, the length of the cable and the normal displacement of the cable from the initial position, respectively. In addition, a denotes the ratio of tension T of the cable to the linear density ρ of the cable, namely $\frac{T}{\rho}$, while a_{x0} represents the ratio of T to the linear density ρ_{x0} of the cable at the position of the robot, namely, $\frac{T}{\rho_{x0}}$.

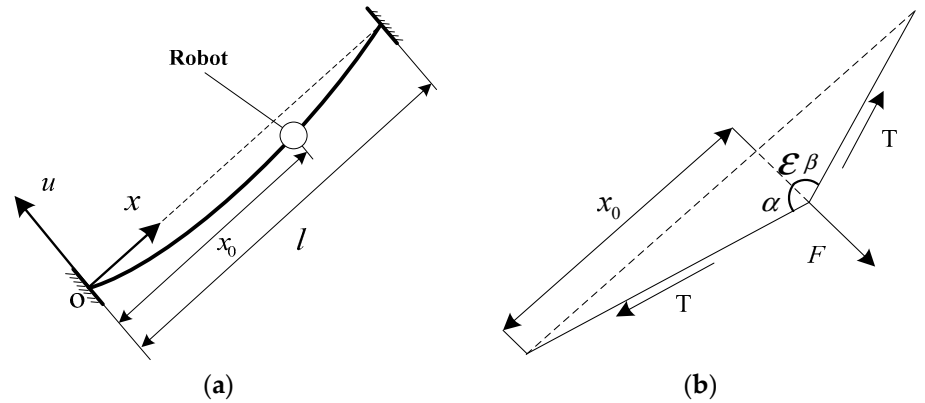

Figure 10. Robot–cable dynamic analysis. (**a**) Schematic diagram of cable vibration; (**b**) Force applied on the robot.

It is difficult to solve string vibration problems when they include a lumped mass. This section adopts an approximate method, namely, the use of the Rayleigh quotient, which can directly estimate the natural frequency of the system without solving its vibration equation. The Rayleigh quotient is expressed in the following form:

$$R = \frac{V_{\max}}{T_{ref}} = \omega_n^2 \tag{19}$$

$V_{\max}$ and T_{ref} represent the maximum potential energy and kinetic energy for reference of the cable respectively, which indicate quantities relating to potential energy and kinetic energy. ω_n denotes the nth-order natural frequency. $V_{\max}$ and T_{ref} can be written as:

$$\begin{cases} V_{\max} = \frac{1}{2}\int_0^l T(W_n'(x))^2 dx \\ T_{ref} = \frac{1}{2}\int_0^l \rho W_n^2(x) dx \end{cases} \tag{20}$$

$W_n(x)$ denotes the nth-order vibration mode function relating to x.

Free vibration of a tensile string is a linear combination of infinite multi-order vibrations. In general, the higher the order is, the smaller the influence on the spectrum, so it is important to study the first-order vibration. Experience shows that the first-order vibration mode of the cable is similar to static deformation under inertial loads. The first-order natural frequency can represent the frequency of the cable, so it is selected as the static deformation of the cable under the self-weight of the robot.

Figure 10b shows that the following equation can be established through the force balance and geometric relationships:

$$\cos(\arctan\frac{x_0}{\varepsilon}) + \cos(\arctan\frac{l - x_0}{\varepsilon}) = \frac{F}{T} \tag{21}$$

where F and ε represent the component of the self-weight of the robot in the vertical direction of the cable and the maximum static deformation, respectively. Because the distance from the position of maximum deformation to the end on the cable changes linearly, the vibration mode function can be obtained as long as ε is known from the following equation:

$$W(x) = \begin{cases} \varepsilon\frac{x}{x_0} & ,0 < x < x_0 \\ \varepsilon\frac{l-x}{l-x_0} & ,x_0 < x < l \end{cases} \tag{22}$$

Therefore, the relationship between x_0 and ε is established according to Equation (21).

$$\cos(\arctan\frac{x_0}{\varepsilon}) + \cos(\arctan\frac{115 - x_0}{\varepsilon}) = \frac{1}{45,300} \tag{23}$$

Based on this, an expression describing the deformation ε through the position of the robot is established, which is to say, $\varepsilon = f(x_0)$. Through data fitting, the samples are obtained such that $x_0 = [0,\ 20,\ 40,\ 60,\ 80,\ 100,\ 115]$. At two ends (0 m and 115 m), the deformation is zero. In view of the sample point being in the middle, the dichotomy is utilized for calculation purposes. In accordance with the zero point theorem, the search interval always shrunk. In this way, the root of the equation can be approached as close as possible. The flowchart of this dichotomy is shown in Figure 11. It is assumed that the self-weight of the robot, tensile force, length and linear density of the cable are G − 200N (including loads), T = 4530 kN, $l = 115$ m and $\rho = 65.6$ kg/m, respectively.

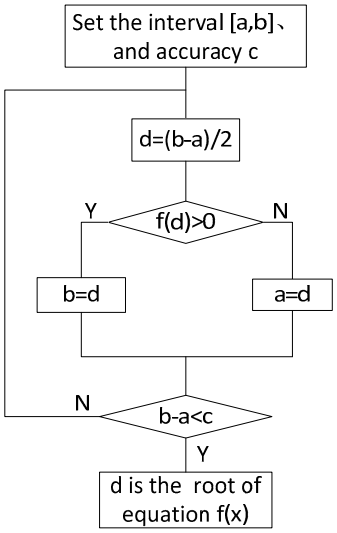

Figure 11. Flow chart of the dichotomy.

The search interval is set to $[0.0001,\ 0.01]$. It is assumed that $f(\varepsilon) = 45,300[\cos(\arctan\frac{x_0}{\varepsilon}) + \cos(\arctan\frac{115-x_0}{\varepsilon})] - 1$ and $f(\varepsilon)$ is the continuous elementary function in the interval. Moreover, for $x_0 = [20,\ 40,\ 60,\ 80,\ 100]$, there exists $f(0.0001) < 0$ and $f(0.001) > 0$. According to the zero point theorem, there are solutions in the interval.

Through calculation, the solutions correspond to $x_0 = [20,\ 40,\ 60,\ 80,\ 100]$ are $[0.0003653,\ 0.0005755,\ 0.0006336,\ 0.0005381,\ 0.0002879]$. Therefore, it is obvious that the weight of the robot affects the cable, albeit only slightly.

As shown in Figure 12a, the distribution of sample points is parabolic. We can get the following equation with quadratic polynomial fitting technique:

$$\varepsilon = 10^{-4}(-0.0019x_0^2 + 0.2208x_0 + 0.0008) \tag{24}$$

Combining the above equation with Equations (22) and (23), the vibration mode function of the robot is:

$$W(x) = \begin{cases} 10^{-4}(-0.0019x_0^2 + 0.2208x_0 + 0.0008)\frac{x}{x_0} & ,0 < x < x_0 \\ 10^{-4}(-0.0019x_0^2 + 0.2208x_0 + 0.0008)\frac{l-x}{l-x_0} & ,x_0 < x < l \end{cases} \tag{25}$$

The first-order frequency is calculated according to Equations (19) and (20). For the cable with its lumped mass, the kinetic energy for reference is obtained:

$$T_{ref} = \frac{1}{2}\int_0^l \rho W^2(x)dx + \frac{1}{2}m[W(x_0)]^2 \tag{26}$$

where m represents the mass of the robot.

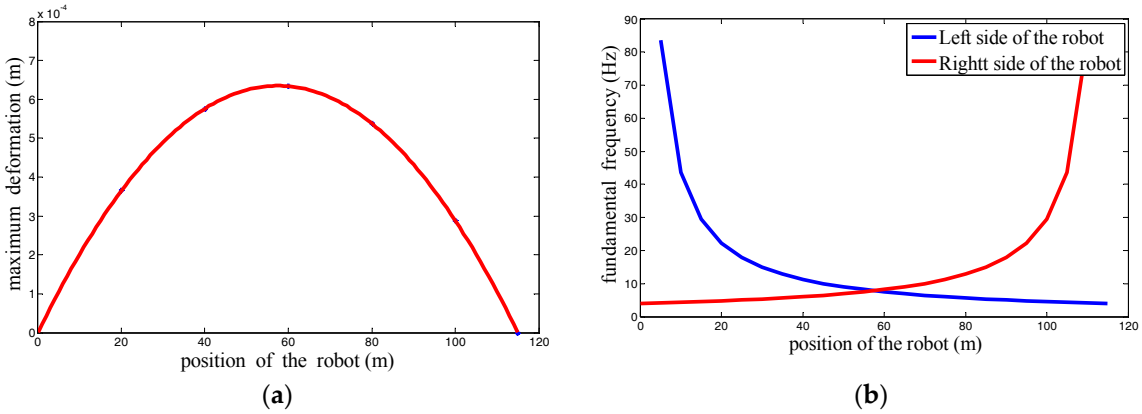

Figure 12. Simulation results: cable deformation and frequency. (**a**) The relationship between the position of the robot and the maximum deformation; (**b**) The change in fundamental frequency of the cable.

As illustrated in Figure 12b, the range of changes in the fundamental frequency of the cable is always less than 90 Hz, showing large differences across the first five fundamental frequencies of the robot rack, so resonance does not occur.

5. Climbing Experiment of the Robot Prototype

To verify the climbing ability of the robot, we fabricated a prototype of the robot, set-up a test platform for the robot and completed climbing & loading experiment of the robot.

5.1. Preparation of the Robot Prototype

According to the structural model of the robot described in Section 2, a prototype of the climbing robot was designed (Figure 13). A current (DC) motor system with high volume and torque was selected as power producer, which include a DC motor, a reducer and a rotary encoder. Based on the model in Figure 1, multiple synchronous pulleys and two synchronous belts were added. Motor 1 drove rolling wheels A and C through synchronous pulleys and belts, while rolling wheel B was driven by motor 2 through synchronous pulleys and belts, to form the all-wheel-drive mechanism climbing along the cable.

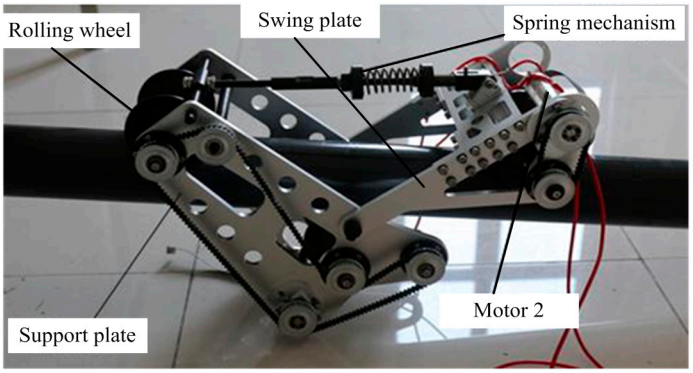

Figure 13. Three-wheel climbing robot.

Through the relative rotation of the swing plates and support plates, scaling of spring and adjustment of spacing between the left and right rolling wheels, the robot could fit around cables of different diameters.

5.2. Vibration Test Platform

By establishing a set of rigid and flexible hybrid robot test platforms, climbing tests using the robot in static and vibration environments was simulated. The vibration test platform is comprised of a simulated cable, fixtures, a vibration table, a lower rigidly-fixed fixture and an upper flexibly-fixed fixture (Figure 14). A hard plastic tube with a diameter of 90 mm was selected to replace the cable and the surface friction coefficient of the tube is similar to that of a typical cable.

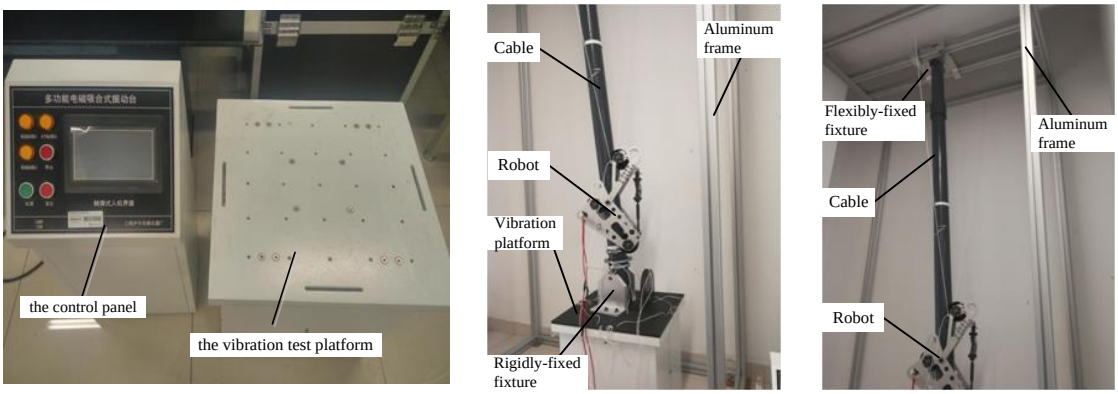

Figure 14. Vibration test platform. (**a**) Electromagnetic vibrator; (**b**) Lower rigidly-fixed fixture; (**c**) Upper flexibly-fixed fixture.

The lower rigidly-fixed fixture was mounted on the vibration table and connected to the lower end of the cable with a fixed hinge, which accurately transferred vibration and adjusted the inclination angle of the cable according to the need. A flexible connection was applied to the upper end of the cable and the upper fixture and ropes and spring were used for fixing. The cable and the upper fixture did not make complete contact and vibrated (within a fixed range of amplitudes) to simulate the vibration of real bridge cables.

By using an electromagnetic absorption type of vibration table to drive the cable vibration, the actual vibration of a cable on a bridge was simulated. The vibration table can bear 100 kg and the maximum vibration amplitude was 5 mm. Moreover, the frequency was adjustable in the range from 1 Hz to 400 Hz. The parameters of the electromagnetic vibrator are shown in Table 2.

Table 2. Parameters of the electromagnetic vibrators.

Maximum load: 100 kg	**Power**: 0.75 KW~2.2 KW
Maximum acceleration: <20 g	**The vibration direction**: X + Y + Z
Maximum amplitude: 0~5 mm	**Precision**: 0.01 HZ
Frequency range: 1~400 HZ	**Frequency sweep**: 1~400 HZ

By setting the low and high frequencies used, as well as the low and high vibration intensities of the vibrator, the frequency and amplitude of the cable, as well as the dead time at various frequencies and amplitudes, could be controlled. The main steps involved are as follows:

(1) First, the regions on the cable where the robot can stably grasp onto were explored and marked. The positions of the robot were adjusted so that all the wheels can stably grasp the cable under the influence of the driving forces.
(2) Then, the high-speed camera system and the vibrator were started and debugged.
(3) Main test started. The high-speed camera was used to record various parameters (output frequency and amplitude of the vibrators) and the output frequency and intensity of the test platform when the robot is climbing on the cable, before and after imposing the driving forces.

5.3. Testing Experiment

According to the analysis in Section 3 and for the given diameter of the cable together with those parameters, such as the clamping force of the robot, spacing of the rolling wheels and pre-tightening force of the spring were adjusted. The space between the left and right half-wheels was adjusted to be 42 mm.

As shown in Figure 15, a climbing test was conducted on the robot. Although the surface was smooth and there were obstacles (less than 10 mm in height), the robot could climb in a stable manner. By selecting heavy objects (mass, 10 kg), the climbing ability of the robot with loads was verified. The robot could still climb normally under such loads. The test proved that the climbing speed of the robot met the required performance for cable inspection. The following conclusions were drawn by combining simulation and test, data:

(1) When masses of 10 kg were added to the robot, the robot could still climb along cables with inclination angle between 20° to 90°.
(2) The robot could be installed and maintained by only one worker.
(3) The climbing speed could be adjusted within the range from 0 m/s to 0.164 m/s.
(4) The robot could pass across obstacles over a maximum length of 10 mm.

(**a**) (**b**) (**c**)

Figure 15. Climbing test of the robot. (**a**) Climbing on the smooth surface; (**b**) Climbing on the surface with obstacles; (**c**) Load test.

The climbing ability of the robot under the low-frequency and high-frequency vibration was further investigated and parameters, such as vibration direction, frequency and intensity of the vibration table could be adjusted through a controller. Based on the combined vibration in horizontal and vertical directions, the test was conducted using the combination of frequencies of 10 Hz and 100 Hz and vibration intensities of 20%, 40% and 60% (namely, 1 mm, 2 mm and 3 mm) of the maximum amplitude. The test shows that the robot could climb normally and its driving wheels did not skid. As a result, it did not leave the cable under the influence of inertial force during the vibration testing. Meanwhile, when the vibration table worked at a low frequency, the whole test system vibrated strongly, which exceeded the bearing limit of the floor of the building and limited the applicable test range. This should be addressed before in the future research.

6. Conclusions

In view of automatic inspection demands for bridge cables at high altitude, the all-wheel-drive climbing robot based on safety recovery mechanism model was developed. On this basis, this work analyzed the climbing performance and fabricated a prototype on which verification testing was conducted. The main conclusions are as follows:

(1) In order to limit the excessive speed of the robot when it is in electrical fault, the centrifugal–friction recovery mechanism model of the all-wheel-drive climbing robot is designed.
(2) The climbing performances of the robot are analyzed, including basic climbing conditions under minimum output motor torque and minimum friction force on the rolling wheels.
(3) By using the finite element method, the natural frequency of the robot was found and the first five modal frequencies were 322 Hz, 463 Hz, 606 Hz, 723 Hz and 911 Hz. Furthermore, the natural frequency of the cable was obtained by using the Rayleigh quotient. The results show that the change in fundamental frequency of the cable was always less than 90 Hz, showing significant differences with the first five modal frequencies of the robot, so resonance did not occur, thus ensuring the safety of the robot–cable system.
(4) The prototype of the robot is made and complete climbing & loading testing experiments is conducted. The testing results proved that the robot can carry a payload of 10 kg and safely return the cable under the influences of inertial force and vibration at the combination of frequencies of 10 Hz and 100 Hz and intensities accounting for 20%, 40% and 60% (namely, 1 mm, 2 mm and 3 mm) of the maximum vibration amplitude. This proved the feasibility of the robot.

In future research, it is necessary to optimize the mechanical structure of the robot, propose more accurate control methods and study inspection methods which are better suited for detection of defects in different cables.

Author Contributions: Data curation, F.X. and L.Z.; Formal analysis, F.X. and M.W.; Investigation, F.X.; Methodology, Q.J. and F.L.; Writing—original draft, F.X.; Writing—review & editing, Q.J.

Funding: This research was funded by [National Natural Science Foundation of China] grant number [51775284], [Primary Research & Development Plan of Jiangsu Province] grant number [BE2018734], [State Key Laboratory of Robotics and System (HIT)] grant number [SKLRS-2017-KF-10], [Jiangsu Six Talent Peaks Program] grant number [JY-081] and [Joint Research Fund for Overseas Chinese, Hong Kong and Macao Young Scholars] grant number [61728302].

Conflicts of Interest: The authors declare no conflict of interest.

References

1. Cho, K.H.; Jin, Y.H.; Kim, H.M.; Moon, H.; Koo, J.C.; Choi, H.R. Multifunctional Robotic Crawler for Inspection of Suspension Bridge Hanger Cables: Mechanism Design and Performance Validation. *IEEE/ASME Trans. Mechatron.* **2017**, *22*, 236–246. [CrossRef]
2. Cho, K.H.; Kim, H.M.; Jin, Y.H.; Liu, F.; Moon, H.; Koo, J.C.; Choi, H.R. Inspection Robot for Hanger Cable of Suspension Bridge: Mechanism Design and Analysis. *IEEE/ASME Trans. Mechatron.* **2013**, *18*, 1665–1674. [CrossRef]
3. Kim, J.W.; Lee, C.; Park, S.; Lee, J.J. Magnetic flux leakage-based steel cable NDE and damage visualization on a cable climbing robot. *Proc. SPIE* **2012**, *8345*, 46.
4. Park, S.; Kim, J.W.; Lee, C.; Lee, J.J. Magnetic Flux Leakage Sensing-Based Steel Cable NDE Technique. *Shock. Vib.* **2014**, *5*, 1–8. [CrossRef]
5. Ho, H.-N.; Kim, K.-D.; Park, Y.-S.; Lee, J.-J. An efficient image-based damage detection for cable surface in cable-stayed bridges. *NDT & E Int.* **2013**, *58*, 18–23.
6. Luo, J.; Xie, S.R.; Gong, Z.B. Development of cable maintenance robot for cable-stayed bridges. *Ind. Robot. Int. J.* **2007**, *34*, 303–309. [CrossRef]
7. Tavakoli, M.; Marques, L.; Almeida, A. A low-cost approach for self-calibration of climbing robots. *Robotica* **2011**, *29*, 23–34. [CrossRef]
8. Zhu, H.; Gu, S.; He, L.; Guan, Y.; Zhang, H. Transition Analysis and Its Application to Global Path Determination for a Biped Climbing Robot. *Appl. Sci.* **2018**, *8*, 122. [CrossRef]
9. Tavakoli, M.; Cabrita, G.; Faria, R.; Marques, L.; de Almeida, A.T. Cooperative multi-agent mapping of three-dimensional structures for pipeline inspection applications. *Int. J. Robot. Res.* **2012**, *31*, 1489–1503. [CrossRef]

10. Allan, J.F.; Lavoie, S.; Reiher, S.; Lambert, G. Climbing and pole line hardware installation robot for construction of distribution lines. In Proceedings of the 2010 1st International Conference on Applied Robotics for the Power Industry (CARPI), Montreal, QC, Canada, 5–7 October 2010; IEEE: Piscataway, NJ, USA, 2010; pp. 1–5.
11. Li, N.; Ji, X.G.; Xu, K.; Cui, A.Q. A Multi-pose pole-climbing Robot to Adapt Guidebar with Different Diameter. *Mod. Manuf. Eng.* **2011**, *9*, 60–61.
12. Lam, T.L.; Xu, Y. Biologically inspired tree-climbing robot with continuum maneuvering mechanism. *J. Field Robot.* **2012**, *29*, 843–860. [CrossRef]
13. Schempf, H.; Mutschler, E.; Gavaert, A.; Skoptsov, G.; Crowley, W. Visual and Nondestructive Evaluation Inspection of Live Gas Mains Using the ExplorerTM Family of Pipe Robots. *J. Field Robot.* **2010**, *27*, 217–249.
14. Xiao, Z.; Wu, W.; Wu, J.; Zhu, H.; Su, M.; Li, H.; Guan, Y. Gripper Self-Alignment for Autonomous Pole-Grasping with a Biped Climbing Robot. In Proceedings of the IEEE International Conference on Robotics and Biomimetics, Guangzhou, China, 11–14 December 2012; pp. 181–186.
15. Jiang, Q.; Xu, F. Grasping Claws of Bionic Climbing Robot for Rough Wall Surface: Modeling and Analysis. *Appl. Sci.* **2018**, *8*, 14. [CrossRef]
16. Yanagida, T.; Elara Mohan, R.; Pathmakumar, T.; Elangovan, K.; Iwase, M. Design and Implementation of a Shape Shifting Rolling–Crawling–Wall-Climbing Robot. *Appl. Sci.* **2017**, *7*, 342. [CrossRef]
17. Xu, F.; Wang, X. Cable Inspection Robot for Cable-Stayed Bridges: Design, Analysis, and Application. *J. Field Robot.* **2011**, *28*, 441–459. [CrossRef]
18. Xu, F.; Hu, J.L.; Wang, X.; Jiang, G. Helix Cable-Detecting Robot for Cable-Stayed Bridge: Design and Analysis. *Int. J. Robot. Autom.* **2014**, *29*, 406–414. [CrossRef]
19. Xu, F.; Wang, B.; Shen, J.; Hu, J.; Jiang, G. Design and realization of the claw gripper system of a climbing robot. *J. Intell. Robot. Syst.* **2018**, *89*, 301–317. [CrossRef]
20. Han, S.; Ahn, J.; Moon, H. Remotely controlled prehensile locomotion of a two-module 3D pipe-climbing robot. *J. Mech. Sci. Technol.* **2016**, *30*, 1875–1882. [CrossRef]
21. Sadeghi, A.; Moradi, H.; Nil Ahmadabadi, M. Analysis, simulation, and implementation of a human-inspired pole climbing robot. *Robotica* **2012**, *30*, 279–287. [CrossRef]
22. Lee, G.; Kim, H.; Seo, K.; Kim, J.; Kim, H.S. MultiTrack: A multi-linked track robot with suction adhesion for climbing and transition. *Robot. Auton. Syst.* **2015**, *72*, 207–216. [CrossRef]
23. Espinoza, R.V.; Oliveira, A.S.; Arruda, L.V.R.; Junior, F.N. Navigation's stabilization system of a magnetic adherence-based climbing robot. *J. Intell. Robot. Syst.* **2015**, *78*, 65–81. [CrossRef]